Poloidal Flow Generated by Tearing Mode

Nishimura, Seiya
Interdisciplinary Graduate School of Engineering Sciences, Kyushu University

Yagi, Masatoshi
Research Institute for Applied Mechanics, Kyushu University

Ito, Sanae-I.
Research Institute for Applied Mechanics, Kyushu University

Ito, Kimitaka
National Institute for Fusion Science

https://doi.org/10.15017/26835

出版情報：九州大学応用力学研究所所報. 133, pp.81-89, 2007-09. Research Institute for Applied Mechanics, Kyushu University
バージョン：
権利関係：

Poloidal Flow Generated by Tearing Mode

Seiya NISHIMURA *1, Masatoshi YAGI *2, Sanae-I. ITOH*2
and Kimitaka ITOH *3
E-mail of corresponding author: *nseiya@riam.kyushu-u.ac.jp*

(Received July 19, 2007)

Abstract

The nonlinear simulation of collisional drift-tearing mode is performed using the reduced two fluid model, and the characteristics of poloidal flow generated by tearing mode is investigated in the phase of magnetic island formation. It is found that the poloidal flow extends to the outside of magnetic island. It is also found that the ion viscosity is an important parameter to determine the flow pattern.

Key words : *magnetic island, collisional drift-tearing mode, poloidal flow, Maxwell stress, ion viscosity, reduced two fluid model*

1. Introduction

The spontaneous topology change of magnetic field is observed in magnetized plasmas. The magnetic island formation is one prototypical example of structure formation in high temperature plasma. There are some important problems to be resolved.

The control of magnetic island is a crucial issue in the International Thermonuclear Experimental Reactor(ITER); if the magnetic island appears, the confinement degradation occurs, which may prevent the self-ignition. This issue requires progress of understanding from various view points. First, the island can be an origin of collapse events, i.e., the disruption can be caused by the overlap of magnetic islands[1]. Further assessment on the recent work on tearing mode is found in a recent review[2]. Second, the active control of magnetic island is studied with the 'electron cyclotron current drive', which heats the plasma and modifies the bootstrap current to suppress the neoclassical tearing mode[3]. Third, the coupling of the tearing mode with the pressure stimulates studies in wider circumstances of configurations, and the characteristics of static magnetic island is intensively investigated in the helical devices[4]. Fourth, the magnetic island also influences the meso-scale poloidal flow, such as zonal flows[5, 6], and a new route of the influence of islands on confinement is searched for[7]. The flattening of pressure profile is well known, and recently the poloidal flow in the island is also measured in the herical device[8].

It has been often believed that the tearing mode is linearly stable in high temperature tokamak plasmas and there exists external drive to excite magnetic island nonlinearly(see review 2)). Indeed, the sawtooth collapse and the edge localized mode[9] sometimes trigger the neoclassical tearing mode. However, the magnetic island appears without clear trigger events in some cases[10]. These observations lead to two working hypothesis. In the first line of thought, it is suggested that the linear tearing mode might be unstable so as to explain the trigger-less excitation of magnetic island[11]. Then, the experimental observation of current profile, which determines the linear stability of tearing mode, should be evaluated more accurately in toroidal geometry. In addition, the analysis of tearing mode in the collisionless regime (including electron inertia and dynamic neoclassical viscosity) is necessary. The alternative way of thought is to take into account the coupling with the background microscopic turbulence. Possibility has been pointed out that a stable neoclassical tearing mode can be excited by background turbulence, based on the theory[12, 13] and on the nonlinear simulation[14].

In the theoretical research, much works has been done for the neoclassical tearing mode. Saturation level of magnetic island seems to be explained[2, 11, 15], but trigger mechanism requires further research. The influence of the island on transport has not yet been fully understood. The interaction between magnetic island and drift waves has been investigated in the context of the drift-tearing mode[16, 17]. This model describes the coexistence of linearly unstable tearing mode and

*1 Interdisciplinary Graduate School of Engineering Sciences, Kyushu University
*2 Research Institute for Applied Mechanics, Kyushu University
*3 National Institute for Fusion Science

linearly stable drift waves. It is known that the drift-tearing mode describes the characteristics of magnetic island observed in experiments, for instance, flattening of the pressure gradient and generation of the poloidal flow[17, 18]. Such modifications of equilibrium profile is significant for the confinement degradation, and they also affect the threshold of other instabilities in the peripheral region of the island. Surveying the proceeding simulations on drift-tearing mode, the pressure flattening effect was analyzed in simulation results. However, the generation of poloidal flow has not been subject to attentions so much.

Our motivation of this study is as follows. The anomalous transport in tokamak plasmas is dominated by the turbulence. The intensity of flux is determined by the competition between turbulence and zonal flow[5]. The importance of the Maxwell stress, in addition to the Reynolds stress, has been pointed out, as was reviewed in 5). In addition, the oscillation of geodesic acoustic mode(GAM) is thought to be important for turbulent transport. Since the GAM absorbs the energy of the zonal flow, then the turbulent transport is excited[19]. By analogy with this, the poloidal flow generated by magnetic island might interact with the zonal flow and modifies the turbulent transport. On the view point of multi-scale interaction between turbulent transport and MHD, the flow generation should be examined in detail.

In this paper, the nonlinear simulation of collisional drift-tearing mode is performed, and the generation mechanism and the characteristics of poloidal flow generated by magnetic island is investigated, using the reduced two fluid model. In § 2, we introduce our model equations. In § 3, the nonlinear simulation of collisional drift-tearing mode is performed, and characteristics of poloidal flow is discussed. In addition, the angular momentum of poloidal flow and the transport by collisional drift-tearing mode are shown. § 4 is devoted to summary and discussion.

2. Model Equations

In this paper, the linear stability and the nonlinear evolution of collisional drift-tearing mode are investigated using the reduced set of two-fluid equations[18], which is derived from Braginskii's two fluid equations. In large tokamak plasmas such as JT-60U, the collisional frequency is sufficiently small, so that the collisionless drift-tearing mode should be considered[20]. However, we are interested in the generation of poloidal flow followed by the magnetic island formation not linear stability, so that we will analyze collisional drift-tearing mode as a first step.

We consider the cylindrical plasma coordinates (r, θ, z) stand for the radius, the poloidal angle and the toroidal position. Variables, notations and the the normalization are almost the same as those in our previous work[21], here we briefly explain model equations. The model equations are written as:

$$\frac{D}{Dt}\nabla_\perp^2\phi = \nabla_\parallel j_\parallel + \mu\nabla_\perp^4\phi, \tag{1}$$

$$\frac{\partial}{\partial t}A = -\nabla_\parallel(\phi - \delta p) - \eta_\parallel j_\parallel + \alpha_T\delta\nabla_\parallel T, \tag{2}$$

$$\frac{D}{Dt}n + \beta_s\frac{D}{Dt}p = \delta\beta\nabla_\parallel j_\parallel + \eta_\perp\beta\nabla_\perp^2 p, \tag{3}$$

$$\frac{3}{2}\frac{D}{Dt}T - \frac{D}{Dt}n = \alpha_T\delta\beta\nabla_\parallel j_\parallel + \epsilon^2\chi_\parallel\nabla_\parallel^2 T + \chi_\perp\nabla_\perp^2 T, \tag{4}$$

and

$$j_\parallel = -\nabla_\perp^2 A,\ p = nT,\ \alpha_T = 0.71,$$

$$\frac{D}{Dt} = \frac{\partial}{\partial t} + [\phi,\ ],\ \nabla_\parallel = \frac{\partial}{\partial z} - [A,\ ],$$

$$\nabla_\perp = \hat{r}\frac{\partial}{\partial r} + \hat{\theta}\frac{1}{r}\frac{\partial}{\partial\theta},\ \ [f,g] = \hat{z}\cdot\nabla f\times\nabla g.$$

Equations (1)-(4) are vorticity equation, generalized Ohm's law, continuity equation and electron heat balance equation, respectively. The variables $\{\phi, A, n, T, p\}$ indicate the electrostatic potential, vector potential parallel to the ambient magnetic field, electron density, electron temperature and electron pressure, respectively. The collisional transport coefficients $\{\mu, \eta_\parallel, \eta_\perp, \chi_\parallel, \chi_\perp\}$ are ion viscosity, parallel resistivity, perpendicular resistivity($\eta_\perp\beta$ implies particle diffusivity), electron parallel thermal conductivity and electron perpendicular thermal conductivity, respectively. We may assume these transport coefficients implicitly include the turbulent transport effect. Quantities $\{\delta, \beta\}$ indicate ion skin depth normalized by the minor radius and plasma beta value at plasma center. β_s is the beta value at the rational surface.

A perturbed quantity $f(\mathbf{x}, t)$ is assumed to vary as:

$$f_0(r) + \sum_{m,n}\tilde{f}_{m,n}(r,t)\exp\{i\,(m\theta - nz)\}, \tag{5}$$

in the cylindrical coordinates (Fourier expansion in θ and z directions). m is a poloidal mode number and n is a toroidal mode number. In our normalization, the center and the edge of plasma corresponds to $r = 0$ and $r = 1$, respectively. The perturbation $\tilde{f}_{m,n}(r)$ satisfies the boundary conditions; $\tilde{f}_{m,n}(0) = \tilde{f}_{m,n}(1) = 0$ for $m, n \neq 0$ and $\partial\tilde{f}_{0,0}/\partial r|_{r=0} = \tilde{f}_{0,0}(1) = 0$. In addition, we impose the same boundary conditions to the vorticity $\nabla_\perp^2\tilde{\phi}$ and the current $\tilde{j}_\parallel$.

The energy conservation relation is written as

$$\frac{d}{dt}H = -\mu\langle|\ \nabla_\perp^2\phi\ |^2\rangle - \eta_\parallel\langle j_\parallel^2\rangle - \eta_\perp\langle|\ \nabla_\perp p\ |^2\rangle$$
$$-\frac{\epsilon^2\chi_\parallel}{\beta}\langle|\ \nabla_\parallel T\ |^2\rangle - \frac{\chi_\parallel}{\beta}\langle|\ \nabla_\perp T\ |^2\rangle, \tag{6}$$

where $\langle\ \rangle$ indicates the volume integral and H is Hamiltonian defined as:

$$H = \frac{1}{2}\langle |\nabla_\perp \phi|^2\rangle + \frac{1}{2}\langle |\nabla_\perp A|^2\rangle + \frac{1}{2\beta}\langle n^2\rangle + \frac{3}{4\beta}\langle T^2\rangle + \frac{\beta_s}{2\beta}\langle (n+T)^2\rangle. \quad (7)$$

The electrostatic and electromagnetic energies of (m,n) Fourier mode averaged in the r direction are given by:

$$E_{\tilde{\phi}_{m,n}} = \frac{1}{2}\int_0^1 dr\ |\nabla_\perp \tilde{\phi}_{m,n}|^2, \quad (8)$$

$$E_{\tilde{A}_{m,n}} = \frac{1}{2}\int_0^1 dr\ |\nabla_\perp \tilde{A}_{m,n}|^2\ . \quad (9)$$

The equilibrium quantities are chosen as:

$$q(r) = q_0 + (q_r - q_0)(r/r_s)^3, \quad (10)$$

$$n_0'(r) = -2r\beta/\epsilon, \quad (11)$$

$$T_0'(r) = -2r\beta/\epsilon, \quad (12)$$

$$p_0'(r) = n_0'(r) + T_0'(r), \quad (13)$$

where the prime indicates the radial derivative. $q(r)$ stands for the safety factor. $\{r_s, q_0, q_r, \epsilon\}$ are the radial position of rational surface, the safety factor at plasma center, the safety factor at rational surface and the inverse aspect ratio of plasma, respectively. In this profile, β_s is given by $\beta_s = \beta(1-r_s^2)^2$.

In the numerical calculation, we set $q_0 = 1.5, q_r = 2.0, r_s = 0.6, \epsilon = 0.2, \beta = 0.01$ and $\delta = 0.01$, which are typical values in large size tokamaks. The equilibrium current $j_0(r)$ is evaluated by the cylindrical equilibrium. The default value of transport coefficients are chosen as $\mu = 10^{-5}, \eta_\parallel = 10^{-5}, \eta_\perp = 2\times 10^{-5}, \chi_\parallel = 10^0, \chi_\perp = 10^{-5}$.

In the linear stability analysis, we use the inverse iteration method to solve the eigenvalue problem. For the nonlinear simulation, the predictor-corrector scheme is adopted to calculate the time evolution, and the spectral method is used to evaluate nonlinear terms. For the simplicity, we consider the resonant mode with single helicity, which satisfies $m/n = 2$. The radial grid is 512 meshes, and the time step is 0.01 for nonlinear calculations.

3. Analysis

3.1 Linear stability analysis

For the preparation of nonlinear simulation, the linear stability analysis is performed using the linearlized model equations, which are given in Ref.[21].

Figure 1 shows the linear growth rate of collisional drift-tearing mode. n indicates the mode number. It is shown that only $(m,n) = (2,1)$ mode is unstable and the drift waves with higher mode number ($(m,n) = (2n,n)$ $(n \geq 2)$) are stable.

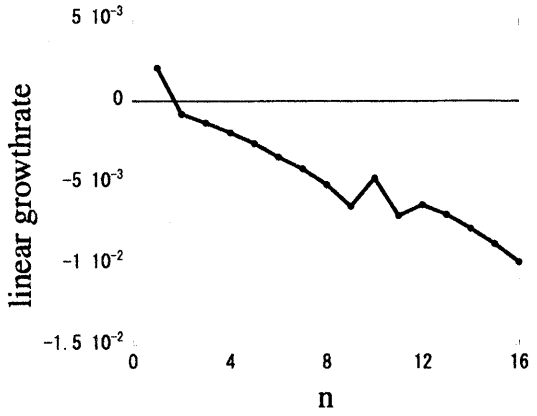

Fig. 1 Mode number dependence of linear growth rate of collisional drift-tearing mode.

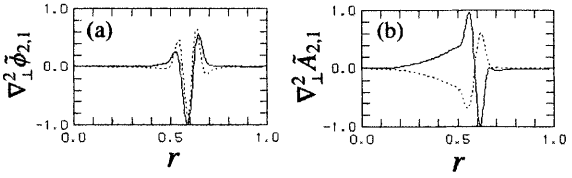

Fig. 2 The eigenfunctions of $(2,1)$ collisional drift-tearing mode; (a) vorticity and (b) current. The solid and dotted lines indicate the real and imaginary parts, respectively.

Figure 2 shows eigenfunction of (2,1) collisional drift-tearing mode, where the vorticity and current are plotted. It is found that the vorticity and the current have real and imaginary parts around the rational surface $r_s = 0.6$, which plays a role to generate the poloidal flow shown in the next subsection.

3.2 Nonlinear simulation

In this subsection, the nonlinear simulation of collisional drift-tearing mode is performed. Firstly, the temporal evolution of magnetic island and the poloidal flow is discussed. The detailed analyses are given in the next two parts.

3.2.1 Temporal evolution of magnetic island and poloidal flow

In the nonlinear simulation, the saturation of magnetic island and generation of poloidal flow are observed.

Figure 3 shows time evolution of $E_{\tilde{A}_{2,1}}$ and $E_{\tilde{\phi}_{0,0}}$. In this case, the vector potential $\tilde{A}_{2,1}$ and the scalar potential $\tilde{\phi}_{0,0}$ correspond to the magnetic island and the

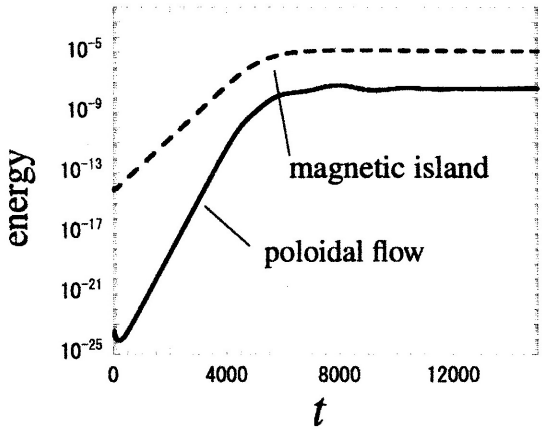

Fig. 3 The time evolutions of magnetic island energy $E_{\tilde{A}_{2,1}}$ and poloidal flow energy $E_{\tilde{\phi}_{0,0}}$.

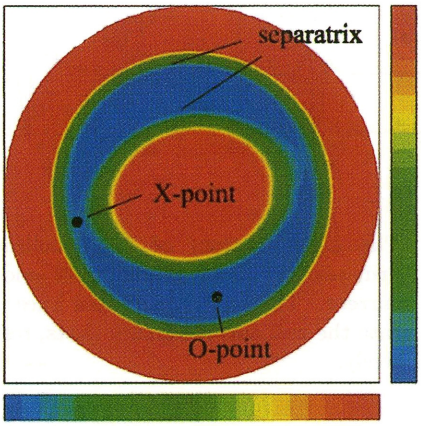

Fig. 4 The contour plot of helical flux function.

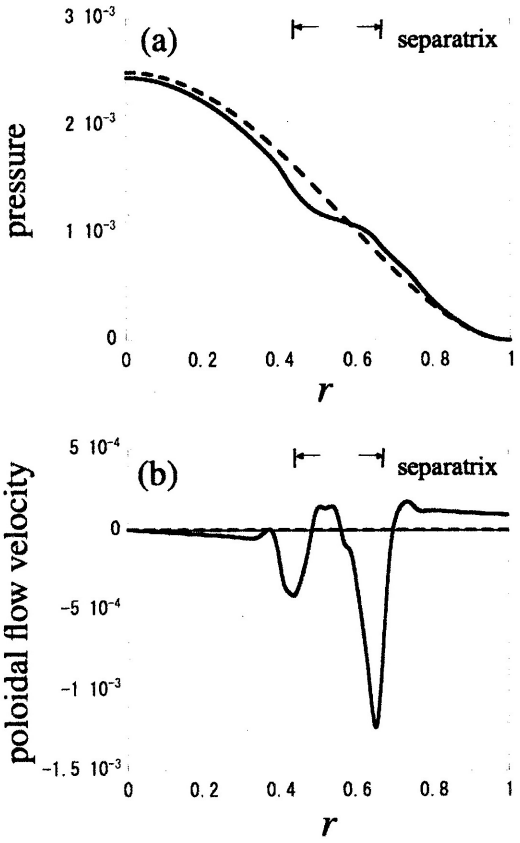

Fig. 5 The radial profiles of equilibrium quantities modified by magnetic island; (a) the pressure and (b) the poloidal flow velocity. The solid and dotted lines indicate the profiles in the initial state and the saturated magnetic island state, respectively.

poloidal flow, respectively. The linear growing phase is between $t = 0$ and $t = 4000$. After $t = 4000$, the so called 'Rutherford regime[22]' is observed. The saturation time of magnetic island is about $t = 8000$ similar to the case of poloidal flow.

Figure 4 indicates the contour plot of helical flux[22] at $t = 12000$ and $z = 0$. The helical flux is defined by:

$$A_*(r,\theta,z) \equiv A_0(r) + \frac{r^2-1}{4} + \tilde{A}_{0,0}(r) + \sum_{m/n=2} \tilde{A}_{m,n}(r) \exp\{i(m\theta - nz)\}, \quad (14)$$

in our normalization, and the contour plot of helical flux describes the topology of perturbed magnetic flux surface. The separatrixes of magnetic island at the maximum width are radially located at $r = 0.44$ and $r = 0.67$. The X-point and the O-point are located at $r = 0.61$ and $r = 0.56$, respectively.

Figure 5 indicates the radial profiles of pressure and poloidal flow velocity. The poloidal flow velocity is given by:

$$v_\theta = \frac{\partial \tilde{\phi}_{0,0}}{\partial r}, \quad (15)$$

which is the θ component of $E \times B$ drift velocity in our normalization. The initial conditions are represented by broken lines, and the solid lines shows the profiles at the state where magnetic island is saturated. It is observed that the pressure gradient inside the separatrix is flattened by magnetic island(the residual gradient of the pressure gradient on the magnetic island is owing to the fact that the thermal conduction is kept finite in this simulation). The poloidal flow has the radial nodes, and extends out the separatrix.

It is found that the saturation amplitude of magnetic island are not strongly affected by the poloidal flow.

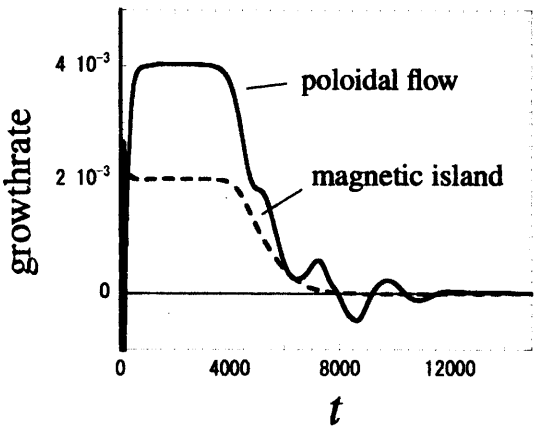

Fig. 6 The time evolutions of magnetic island and poloidal flow growth rate.

3.2.2 Poloidal flow generation

Next, we investigate the generation mechanism of poloidal flow.

Figure 6 shows time evolution of magnetic island and poloidal flow growth rate. The growth rates γ are calculated by the data of Fig.3, using the definition $2\gamma = (\partial/\partial t) \ln X$ (where X is either for magnetic perturbation energy or flow energy).

The growth rate of poloidal flow is just double of that of magnetic island which implies the poloidal flow is generated by the quasi-linear effect of magnetic island perturbation. This is explained as follows. The $(0,0)$ component of Eq.(1), which indicates the evolution of poloidal flow, is given as:

$$\frac{\partial}{\partial t}\nabla_\perp^2 \tilde{\phi}_{0,0} = -\left[\tilde{\phi}, \nabla_\perp^2 \tilde{\phi}\right]_{0,0} + \left[\tilde{A}, \nabla_\perp^2 \tilde{A}\right]_{0,0} + \mu \nabla_\perp^4 \tilde{\phi}_{0,0}, \tag{16}$$

with

$$\left[f, \nabla_\perp^2 f\right]_{0,0} = Re \sum_{m,n} \left\{ -ik_\theta \frac{\partial}{\partial r} \left(\tilde{f}_{m,n} \nabla_\perp^2 \tilde{f}^*_{m,n} \right) \right\},$$

and $k_\theta = m/r$, where the suffix $*$ indicates the complex conjugate. These brackets produce quasi-linear effects. If $\tilde{\phi}_{2,1}$ has the time dependence of $\exp\{(\gamma + i\omega_r)t\}$ where ω_r is the rotation frequency, the complex conjugate of $\nabla_\perp^2 \tilde{\phi}_{2,1}$ is proportional to $\exp\{(\gamma - i\omega_r)t\}$. So that, the time dependence of bracket is $\exp(2\gamma t)$ and the growth rate of poloidal flow is double of the growth rate of magnetic island, if the flow is driven by the quasi-linear effect. Higher harmonics is driven nonlinearly by the $(2,1)$ mode, so that they have larger growth rate. The flow has twice larger growth rate compared to $(2,1)$ mode. The comparison in Fig.6 shows that the flow is dominantly driven by the $(2,1)$ perturbation that induces magnetic island.

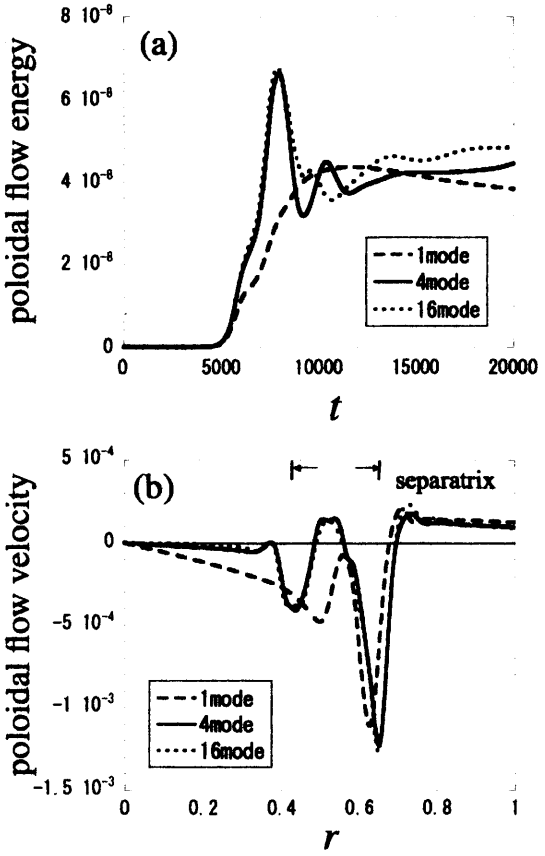

Fig. 7 The number of harmonics dependence of poloidal flow generation; (a) the time evolution of energy and (b) the radial profile of velocity.

Next, the contribution to the quasi-linear effect from higher harmonics is investigated.

Figure 7(a) shows the temporal evolution of poloidal flow energy and (b) the radial structure of poloidal flow with the different number of Fourier harmonics. '1 mode' indicates that we use $(2,1)$ and $(0,0)$ mode in the nonlinear simulation. Similarly, '4 mode' represents the case where $(2,1)$, $(4,2)$, $(6,3)$, $(8,4)$ and $(0,0)$ are retained. In Fig.7(a), the saturation level of poloidal flow energy is not strongly dependent on the number of harmonics. This indicates that the lowest mode number $(2,1)$ dominates the poloidal flow generation, although the fine structure of poloidal flow is modified by the higher harmonics. The radial structure with 4 mode case is almost same as 16 mode case in Fig.7(b), so that we confirm that 4 mode case is sufficient for discussion of poloidal flow generation.

We next demonstrate the role of diamagnetic flow on the turbulence-driven mean poloidal flow.

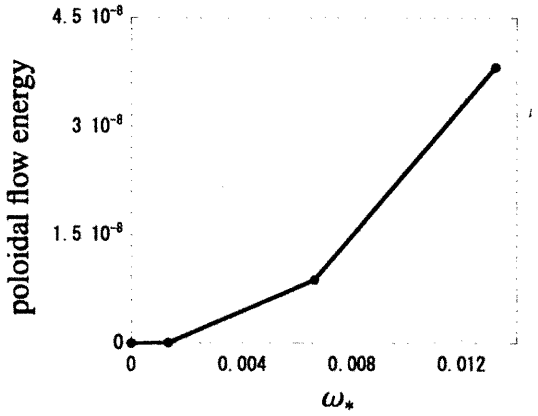

Fig. 8 The initial diamagnetic rotation frequency of $(2,1)$ mode dependence on saturation energy level of poloidal flow.

Figure 8 indicates the dependence of saturation amplitude of poloidal flow energy on the diamagnetic rotation frequency of $(2,1)$ mode. The diamagnetic frequency is calculated by initial condition of equilibrium temperature and density profile. It is found that the generation of poloidal flow is strongly depend on the diamagnetic effect. In the classical tearing mode ($\omega_* = 0$), the amplitude of perturbed scalar potential and perturbed vector potential have pure real or pure imaginary values. In this condition, brackets in Eq.(16) have no contribution, therefore the poloidal flow is not generated. When the diamagnetic drift frequency has finite value, those amplitude become complex shown as Fig.2, so that the brackets have the contribution to the generation of the poloidal flow.

Next, we investigate the contribution to the generation of poloidal flow from Reynolds and Maxwell stress. Figure 9(a) shows the temporal evolution of poloidal flow energy and (b) the radial structure of poloidal flow. The first term and the second term in R.H.S. of Eq.(16) are called 'Reynolds stress' and 'Maxwell stress', respectively. 'Reynolds type' and 'Maxwell type' in Fig.9 indicate the cases without Maxwell stress and without Reynolds stress in Eq.(16), respectively. In these cases, to keep the energy conservation property, $\left[\tilde{\phi}_{m,n}, \nabla_\perp^2 \tilde{\phi}_{0,0}\right]$ in the R.H.S. of Eq.(1), and $\nabla_\parallel \tilde{\phi}_{0,0}$ in the R.H.S. of Eq.(2) are also neglected, respectively. 'mix type' indicates the case with both Reynolds stress and Maxwell stress retained. It is found that the saturation level of poloidal flow energy without Reynolds stress or Maxwell stress are larger than that with both terms in Fig.9(a). This result implies that Reynolds stress and Maxwell stress partially cancel each other.

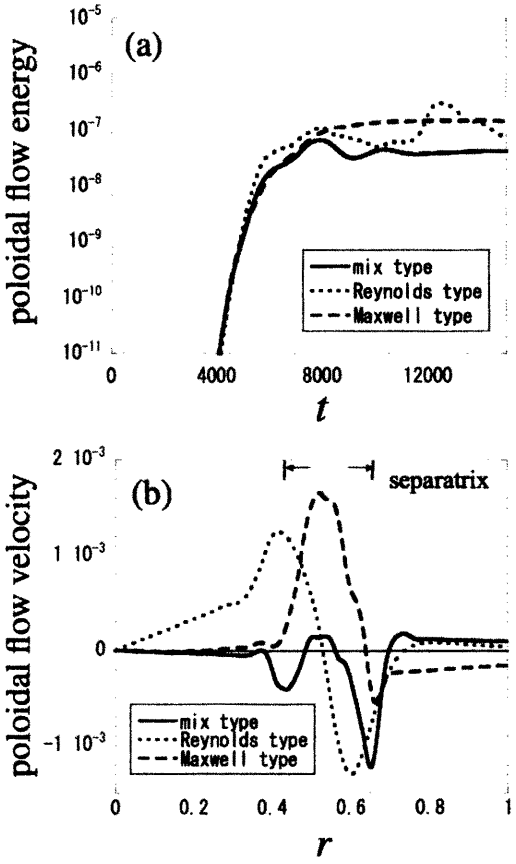

Fig. 9 The three types of poloidal flow; (a) the time evolutions of energy and (b) the radial profiles of velocity.

In the framework of ideal MHD theory, the residue of summation of Reynolds stress and Maxwell stress perfectly vanishes . The radial profile via Reynolds stress approximately has the even parity, on the other hand, Maxwell stress gives the odd parity in the separatrix. The difference of parities between two stress reflects the parity of eigenfunctions in the linear regime (Fig.2).

Figure 10 shows the ion viscosity(μ) dependence of poloidal flow. Three cases are plotted; '1.E-6', '1.E-5' and '1.E-4' represent 10^{-6}, 10^{-5} and 10^{-4}, respectively. In Fig.10(a), as the value of ion viscosity increases, the growth rate of poloidal flow energy becomes small, since the growth rate of $(2,1)$ collisional drift-tearing mode is monotonic decreasing function of ion viscosity in our parameters of interest. The saturation level of poloidal flow energy is also monotonic decreasing function of ion viscosity. According to the increase of ion viscosity, the radial flow pattern changes. Comparing radial structure in cases with '$\mu = 1.E-6$' and '$\mu = 1.E-4$', it is found that they roughly have the odd parity and the

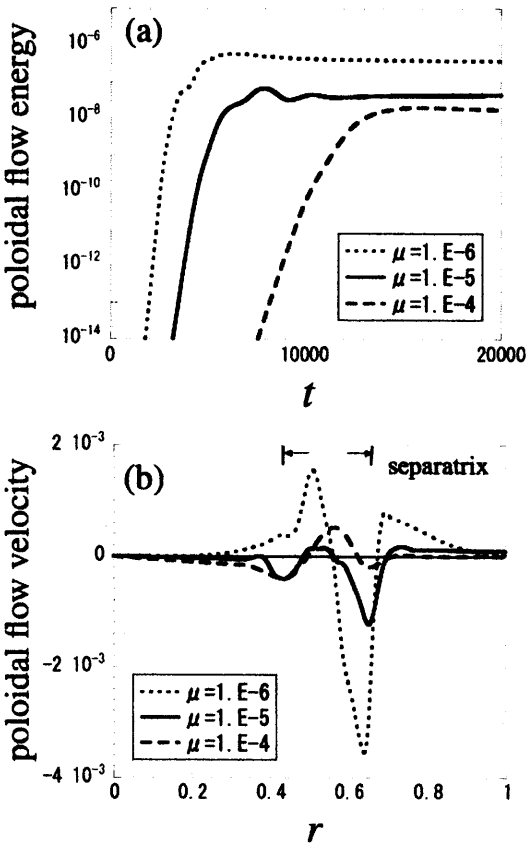

Fig. 10 The ion viscosity dependence of poloidal flow; (a) the time evolutions of energy and (b) the radial profiles of velocity.

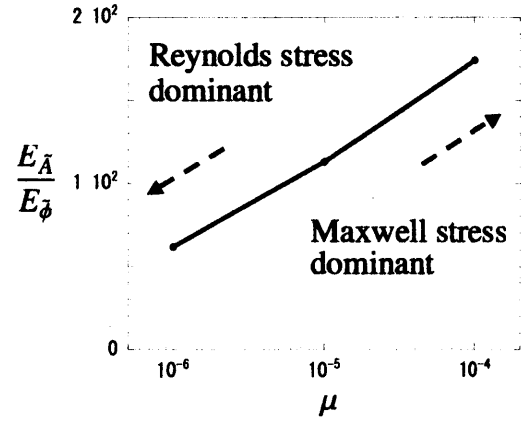

Fig. 11 The ion viscosity dependence of the ratio between the fluctuating energy of vector potential and that of scalar potential.

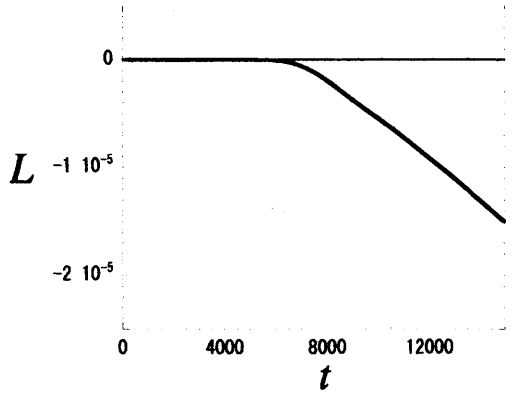

Fig. 12 The time evolution of total angular momentum of poloidal flow.

even parity in the separatrix, respectively. There is a similarity between Fig.9(b) and Fig.10(b).

Figure 11 shows the ion viscosity dependence of the ratio of fluctuating vector potential energy and fluctuating scalar potential energy $E_{\tilde{A}}/E_{\tilde{\phi}}$. Here, the fluctuating energy is calculated by the summation of each energy except (0,0) mode. Each component consisting Reynolds stress:

$$Re\left\{-ik_\theta \frac{\partial}{\partial r}\left(\tilde{\phi}_{m,n}\nabla_\perp^2 \tilde{\phi}^*_{m,n}\right)\right\}, \qquad (17)$$

is approximately proportional to each fluctuating energy of scalar potential $E_{\tilde{\phi}_{m,n}}$, and so is the Maxwell stress. The ratio $E_{\tilde{A}}/E_{\tilde{\phi}}$ monotonically increases with the ion viscosity. This implies that as the ion viscosity becomes larger, the strength of Maxwell stress becomes stronger. On the other hand, the strength of Reynolds stress becomes stronger when the ion viscosity is small. This tendency explains the similarity between Fig.9(b) and Fig.10(b). The competition between Reynolds stress and Maxwell stress is essential to determine the radial structure of poloidal flow pattern and ion viscosity is a nob to control them.

3.2.3 Angular momentum of poloidal flow

Here, we discuss the total angular momentum of poloidal flow.

Figure 12 shows the time evolution of total angular momentum of poloidal flow. it is found that the total angular momentum monotonically decreases with time. The total angular momentum of poloidal flow L is defined by:

$$L = \int_0^1 dr\, r^2 v_\theta, \qquad (18)$$

in the cylindrical coordinate. To clarify the mechanism

of change in the total angular momentum, we derive the analytic formula of time evolution of total angular momentum, which is derived from Eq.(16). Operating $\int_0^r dr\, r$ on both side of Eq.(16), we get:

$$\frac{\partial}{\partial t}(rv_\theta) = -\int_0^r dr\, r\left\{\left[\tilde{\phi}, \nabla_\perp^2 \tilde{\phi}\right]_{0,0} - \left[\tilde{A}, \nabla_\perp^2 \tilde{A}\right]_{0,0}\right\} + \mu\left\{r\frac{\partial}{\partial r}\left(\frac{1}{r}\frac{\partial v_\theta}{\partial r}\right)\right\}. \quad (19)$$

Besides, integrating Eq.(19) over the volume, i.e. operating $\int_0^1 dr\, r$ on both side of Eq.(19), the time evolution of total angular momentum is given by:

$$\frac{\partial}{\partial t}L = \mu\left(r^2\frac{\partial^2\tilde{\phi}_{0,0}}{\partial r^2} - r\frac{\partial\tilde{\phi}_{0,0}}{\partial r}\right)\Big|_{r=1} = -2\mu v_\theta\,|_{r=1}\,, \quad (20)$$

where we use the boundary condition of $\tilde{\phi}_{0,0}$ and $\nabla_\perp^2\tilde{\phi}_{0,0}$ to reach the second line. It can be shown that the terms related with Reynolds stress and Maxwell stress vanish, because of the boundary conditions of amplitude of perturbed scalar potential and perturbed vector potential. Therefore, the total angular momentum is altered by the torque which is caused by the friction between plasma and outside boundary. We confirm that Eq.(20) reproduces the evolution of total angular momentum shown in Fig.12.

3.2.4 Transport by drift-tearing mode

Finally, we investigate the heat transport driven by the collisional drift-tearing mode, which is caused by nonlinear mechanism of tearing mode.

Figure 13(a) shows the power spectrums of averaged heat flux, where n represents the mode number. The heat flux is defined by the product of radial $E \times B$ drift velocity and fluctuating temperature as:

$$\Gamma_n = Re\left\{-ik_\theta\tilde{\phi}_{m,n}\tilde{T}_{m,n}\right\}. \quad (21)$$

The absolute value of radially averaged heat flux is plotted in Fig.13(a). It is found that the low modes are dominant and the high modes are ineffective in the heat transport. This result implies that the drift wave(with high mode numbers) does not grow to large amplitude. To evaluate the impact of this nonlinearly induced heat transport, the spectrum of perturbed temperature amplitude is plotted in Fig.13(b) and is compared with the reference(mixing length estimate). The 'mixing length' indicates the mixing length estimation of perturbed temperature amplitude, which corresponds to the saturation level of unstable drift wave. The mixing length theory is represented by:

$$\frac{\tilde{T}_{m,n}}{T_0} \sim \frac{1}{k_\perp L_T}, \quad (22)$$

and this value is used as a reference. In Fig.13(b), we set $T_0 \sim \beta/\epsilon$, $L_T = 1$ and $k_\perp \sim k_\theta$. It is found that the heat flux by micro modes in the numerical result is much smaller than reference in the high mode number regime. Therefore, it is concluded that the weak heat transport of high mode number is due to the low amplitude of nonlinearly driven drift wave.

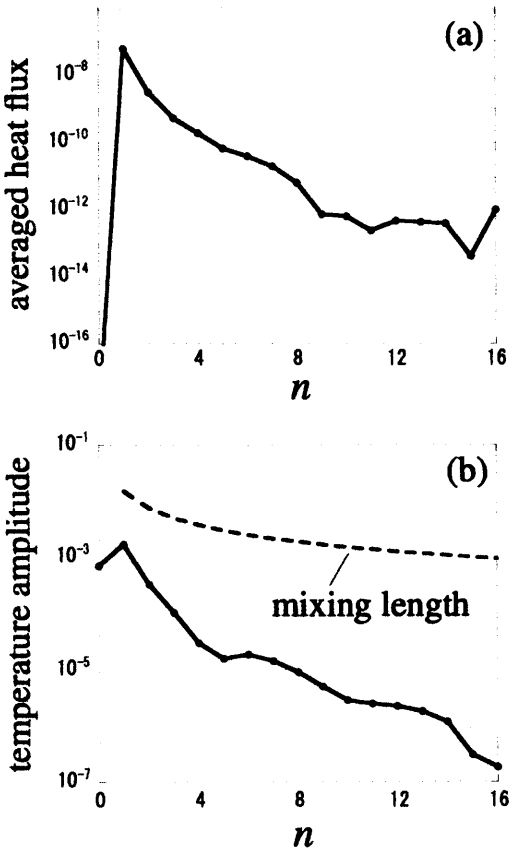

Fig. 13 The power spectrums of (a) averaged heat flux and (b) perturbed temperature.

4. Summery and Discussion

We introduce the reduced two fluid equations which can describe the synergy of magnetic island and drift wave turbulence(so called the collisional drift-tearing mode). Using the reduced two fluid equations, the linear stability analysis of collisional drift-tearing mode and the nonlinear simulation of drift-tearing mode are performed.

In the linear stability analysis, we show that only the lowest mode is unstable, and other high mode number perturbations are completely stable in our parameter of interest. The deference of parity around rational surface between the vorticity and the current of unstable mode is observed.

In the nonlinear simulation, the saturation of magnetic island is observed. In addition, accompanying the formation of magnetic island, the pressure is flattened in the separatrix of magnetic island, and the poloidal flow is generated. In particular, the radial profile of poloidal flow velocity extends to the outside of separatrix.

Then, the generation mechanism and the characteristics of poloidal flow is analyzed. It is found that the poloidal flow is mainly generated by unstable magnetic island perturbation through the quasi-linear effect. In this mechanism, the diamagnetic drift rotation is the origin of poloidal flow generation. Next, the contribution of Reynolds stress and Maxwell stress in Eq.(16) are investigated, then radial pattern of poloidal flow is categorized into three cases; the Reynolds type, the Maxwell type and the mixture of them. Surveying the ion viscosity dependence of radial poloidal flow pattern, the change of poloidal flow pattern from Reynolds type to Maxwell type is observed. This is caused by the changing of fluctuation energy of scalar potential and vector potential, which represent the strength of Reynolds stress and Maxwell stress. Then, we confirmed that the ion viscosity dominates the flow pattern of poloidal flow. The other transport coefficient dependence of poloidal flow is left as a future work.

Next, we investigate the angular momentum of poloidal flow. It is found that the total angular momentum of poloidal flow is changed together with the time evolution. We derived the analytic formula of total angular momentum evolution and confirmed that it is caused by the friction between plasma and outside boundary.

Finally, we discuss the nature of drift wave in our simulation. It is found that the heat transport by the stable drift wave is much weaker than that by the magnetic island. This is because the amplitude of drift wave does not sufficiently grow by comparison with unstable drift wave.

Hereafter, the synergy of magnetic island and active(linearly unstable) turbulence should be investigated.

Acknowledgment

The authors would like to thank Prof. A. I. Smolyakov, Prof. S. Benkadda and Prof. P. H. Diamond for useful discussions.

This work is partially supported by the Grant-in-Aid for Specially-promoted Research of Ministry of Education, Culture, Sports, Science and Technology of Japan (16002005) and the Grant-in-Aid for Scientific Research (B) (19360415) and by collaboration program of Research Institute for Applied Mechanics of Kyushu University. We also acknowledge the collaboration program of National Institute for Fusion Science, Japan(NIFS07KOAP017).

References

1) S.-I. Itoh, K. Itoh, H. Zushi, and A. Fukuyama: Plasma Phys. Control. Fusion 40 (1998) 879.

2) R. J. La Haye: Phys. Plasmas 13 (2006) 055501.

3) H. Zohm, G. Gantenbein, F. Leuterer, A. Manini, M. Maraschek, Q. Yu, *et al.*: Nucl. Fusion 47 (2007) 228.

4) S. Inagaki, N. Tamura, K. Ida, Y. Nagayama, K. Kawahata, S. Sudo, T. Morisaki, K. Tanaka, and T. Tokuzawa: Phys. Rev. Lett. 92 (2004) 055002-1.

5) P. H. Diamond, S.-I. Itoh, K. Itoh, and T. S. Hahm: Plasma Phys. Control. Fusion 47 (2005) R35.

6) K. Itoh, *et al.*: Phys. Plasmas 13 (2006) 055502.

7) C. J. McDevitt, and P. H. Diamond: Phys. Plasmas 13 (2006) 032302.

8) K. Ida, *et al.*: Phys. Rev. Lett. 88 (2002) 015002-1.

9) R.J. Buttery, T.C. Hender, D.F. Howell, R.J. La Haye, O. Sauter, D. Testa, *et al.*: Nucl. Fusion 43 (2003) 69.

10) D. A. Kislov, *et al.*: Nucl. Fusion 41 (2001) 1619.

11) H. Reimerdes, O. Sauter, T. Goodman, and A. Pochelon: Phys. Lev. Lett. 88 (2002) 105005-1.

12) S.-I. Itoh, K. Itoh, and M. Yagi: Phys. Rev. Lett 91 (2003) 045003.

13) S.-I. Itoh, K. Itoh, and M. Yagi: Plasma Phys. Control. Fusion 46 (2004) 123.

14) M. Yagi, *et al.*: Nucl. Fusion 45 (2005) 900.

15) D. A. Gates, *et al.*: Nucl. Fusion 37 (1997) 1593.

16) B. D. Scott, A. B. Hassam, and J. F. Drake: Phys. Fluids 28 (1985) 275.

17) H. R. Hicks, B. A. Carreras, and J. A. Holmes: Phys. Fluids 27 (1984) 909.

18) B. D. Scott, J. F. Drake, and A. B. Hassam: Phys. Rev. Lett. 54 (1985) 1027.

19) M. N. Rosenbluth, and F. L. Hinton: Phys. Rev. Lett. 80 (1997) 724.

20) J. F. Drake, Y. C. Lee: Phys. Fluids 20 (1977) 1341.

21) S. Nishimura, M. Yagi, S.-I. Itoh, M. Azumi, and K. Itoh: J. Phys. Soc. Jpn. 76 (2007) 064501-1.

22) P. H. Rutherford: Phys. Fluids 16 (1973) 1903.